Identification of phagocytosis regulators using magnetic genome-wide CRISPR screens

Michael S. Haney[1,*], **Christopher J. Bohlen**[2,7,#,*], **David W Morgens**[1], **James A. Ousey**[1], **Amira A. Barkal**[3], **C. Kimberly Tsui**[1], **Braeden Ego**[1], **Roni Levin**[4], **Roarke Kamber**[1], **Hannah Collins**[2], **Andrew Tucker**[2], **Amy Li**[1], **Daan Vorselen**[5], **Lorenzo Labitigan**[5], **Emily Crane**[1], **Evan Boyle**[1], **Lihua Jiang**[1], **Joanne Chan**[1], **Esther Rincón**[6], **William J. Greenleaf**[1], **Billy Li**[1], **Michael P. Snyder**[1], **Irving L. Weissman**[3], **Julie A. Theriot**[5], **Sean R. Collins**[6], **Ben A. Barres**[2], **Michael C. Bassik**[1,8,#]

[1]Department of Genetics and Stanford University Chemistry, Engineering, and Medicine for Human Health (ChEM-H), Stanford University School of Medicine, Stanford, CA 94305, USA

[2]Department of Neurobiology, Stanford University School of Medicine, Stanford, CA 94305, USA

[3]Institute for Stem Cell Biology, Stanford University School of Medicine, Stanford, California 94305, USA

[4]Department of Biochemistry, University of Toronto, Toronto, Ontario, Canada.

[5]Department of Biochemistry, Stanford University School of Medicine, Stanford, CA, USA.

[6]Department of Microbiology and Molecular Genetics, UC Davis, Davis, CA 95616, USA.

[7]Present address: Department of Neuroscience, Genentech, South San Francisco, CA 94080, USA.

[8]Lead Contact

Summary

Phagocytosis is required for a broad range of physiological functions, from pathogen defense to tissue homeostasis, but mechanisms required for phagocytosis of diverse substrates remain incompletely understood. Here, we develop a rapid magnet-based phenotypic screening strategy, and perform eight genome-wide CRISPR screens in human cells to identify genes regulating phagocytosis of distinct substrates. After validating select hits in focused mini-screens, orthogonal assays and primary human macrophages, we demonstrate that 1) the previously-uncharacterized gene *NHLRC2* is a central player in phagocytosis, regulating RhoA-Rac1 signaling cascades that control actin polymerization and filopodia formation, 2) very long chain fatty acids are essential for efficient phagocytosis of certain substrates, and 3) the previously-uncharacterized Alzheimer's disease-associated gene *TM2D3* can preferentially influence uptake of amyloid-β aggregates. These findings illuminate new regulators and core principles of phagocytosis, and more generally establish an efficient method for unbiased identification of cellular uptake mechanisms across diverse physiological and pathological contexts.

Keywords

Introduction

Phagocytosis serves a critical role in neutralization and termination of pathogens[1], but also contributes to a diverse range of developmental, homeostatic, and non-infectious disease processes, including apoptotic cell clearance, senescent erythrocyte turnover, tumor surveillance, elimination of cellular debris after injury, and synaptic pruning[2–8]. Imbalances in phagocytosis by professional or non-professional phagocytes[9,10] can lead to autoimmunity, developmental deficits, and buildup of toxic protein aggregates[2,4]. Phagocytes utilize distinct surface receptors and signaling cascades to engulf different types of particles[11], and elucidation of additional molecules that make differential contributions across substrates will help enable narrowly-targeted therapeutics for correcting phagocytosis defects in specific diseases.

Depending on the features of the substrate targeted for engulfment, phagocytes utilize a spectrum of signaling cascades to achieve rapid cytoskeletal reorganization and substrate ingestion[11–14]. Much of our understanding about the molecular basis of phagocytosis derives from forward genetic screens in model organisms. Classical apoptotic cell engulfment screens in *C. elegans* identified (among other genes) phagocytic receptors *ced-1* and *ced-6* as well as key signaling intermediates, *ced-5* and *ced-10,* that serve to activate the SCAR/ WAVE complex during apoptotic cell clearance[15,16]. *Ced*-gene human orthologues *DOCK1, CRK, ELMO1,* and *RAC1* have subsequently been shown to perform analogous signaling functions in mammalian SCAR/WAVE recruitment to activated phagocytic receptors[17,18]. Additional organismal forward-genetic screens conducted in fruit flies and zebrafish have both corroborated prior findings and provided novel insights into regulation of phagocytosis[19–22]. RNAi screens in cultured *Drosophila* S2 cells have also identified

numerous phagocytic regulators[23–26], though a systematic screen for regulators of phagocytosis in mammalian cells has not been reported.

The development of the CRISPR/Cas9 system[27–29] has enabled dramatically improved genome-scale knockout screens with high precision in mammalian cells[30–37]. With an appropriate selection strategy, pooled CRISPR screens allow for effective and systematic interrogation of complex cellular processes. While such screens have been used successfully in a number of cases, comparative analysis of genome-scale screens has been limited by the cost and effort required to either grow large panels of cells extensively or to perform FACS-based sorting, which can be expensive and time-consuming.

Here, we describe a strategy for rapid selection of large-scale human cell populations using phagocytic ability as a direct readout, which relies on magnetic separation of cells that have engulfed paramagnetic particles. We conduct eight distinct genome-wide CRISPR screens to investigate mechanisms of phagocytosis for distinct particle types in the macrophage-differentiated human myeloid cell line U937. Together, this work defines multiple pathways central to human cell phagocytosis, and demonstrate a powerful generalizable strategy to use magnetic separation to rapidly identify regulators of phagocytosis for diverse substrates.

Results

A phenotypic screen for regulators of phagocytosis using magnetic separation

In order to systematically investigate the requirements for phagocytosis of a wide range of substrates, we sought to leverage the power and efficiency of pooled CRISPR screening. We selected a human myeloid cell line with phagocytic activity, U937 cells[38], and optimized a differentiation protocol (Supplementary Figs. 1a,b,c) that allowed the cells to robustly phagocytose diverse types of particles in an actin-dependent manner that could be inhibited by cytochalasin D (Supplementary Figs. 1d,e). We then generated a knockout pool of U937 cells by stably expressing Cas9 and introducing a ~200,000 element lentiviral library of sgRNAs targeting every protein-coding gene in the genome with 10 distinct sgRNAs per gene and ~10,000 negative control sgRNAs[32].

To directly probe the dynamic cellular process of phagocytosis, we developed a magnet-based selection strategy in which U937 cells are rapidly separated based on their capacity to phagocytose superparamagnetic substrates. After incubation with superparamagnetic particles, cells are passed through a uniform magnetic field that captures magnetized cells that ingested paramagnetic particles while non-magnetized cells that failed to phagocytose pass through (Fig.1a). Magnet-bound cell fractions were highly-enriched for phagocytosing cells, with even a single superparamagnetic bead conferring sufficient magnetism to capture associated cells on the column (Fig. 1b). Pretreatment of cells with cytochalasin D prevented magnetic capture, suggesting that surface-associated but non-ingested particles are efficiently removed (Supplementary Fig. 1f).

A genome-wide screen recovers canonical and unexpected regulators of phagocytosis

Having established a phenotypic selection assay, we next performed a genome-wide screen for regulators of phagocytosis in duplicate. In our initial screen we exposed a pool ($2.5{\times}10^8$

cells) of differentiated, Cas9-expressing U937 cells containing a genome-wide knockout library to 1.3 μm diameter superparamagnetic beads for a duration (30 min) optimized to allow for subsequent capture of ~80% of the cells on the magnet. Each sorted fraction was preserved and processed separately, allowing direct comparison of sgRNA abundance in magnet-bound versus unbound cellular fractions within each replicate. Importantly, magnetic selection of the large number of cells required for screening was routinely completed in 1–2 hours, at least an order of magnitude faster than fluorescence or survival-based selections at this scale.

After cell separation, sgRNA sequences were recovered from genomic DNA and sequenced to determine the relative enrichment of each sgRNA in bound versus unbound fractions. Gene-level effects were derived using casTLE [39], with top negative and positive regulators showing clear enrichment across multiple sgRNAs relative to the distribution of both non-targeting and safe-targeting negative control sgRNAs (Figure 1c). Analysis of replicate screen data for 1.3 μm diameter carboxy coated beads identified 85 genes at 10% false discovery rate (FDR), including both genes that promote and inhibit particle uptake (Fig. 1d, Supplementary Fig. 1g, Supplementary Tables 1 and 2). Genes enriched in the unbound fraction (denoted by a negative effect score) result in decreased particle uptake when disrupted, and therefore are normally necessary for efficient phagocytosis. Conversely, genes enriched in the bound fraction (denoted by a positive effect score) result in increased particle uptake when disrupted, and therefore normally inhibit phagocytosis. Pathway analysis for the 85 genes discovered as hits in the 1.3 μm bead screen showed strong enrichment of Reactome pathway terms related to phagocytosis and actin polymerization (Fig. 1e, Supplementary Table 1). Indeed, identified genes encompassed a nearly complete actin polymerization cascade known to be essential for phagocytic cup formation, including *RAC1, DOCK2,* five members of the five-subunit SCAR/WAVE complex (*NCKAP1L, WASF2, ABI1, CYFIP1,* and *BRK1*) and five members of the seven-subunit ARP2/3 complex (*ACTR2, ACTR3, APRC2, ARPC3,* and *ARPC4,* Supplementary Fig. 1g).

Beyond canonical phagocytosis machinery, the hits were enriched for biological pathway categories related to positive regulation of mTOR signaling (Fig. 1e, Supplementary Fig. 1g, Supplementary Table 1). The mTOR-associated Ragulator complex and its regulatory target, RagA, were recently identified as strong modifiers of microglial phagocytic flux in a zebrafish screen[22], a finding supported by identification of RagA (*RRAGA)* and three out of 5 members of the Ragulator complex *(LAMTOR2, LAMTOR3,* and *LAMTOR4)* by our screen in human cells (Fig. 1e, Supplementary Fig. 1g). Additionally, our initial screen identified *NPRL2* of the RagA-inhibiting GATOR1 complex as a gene that promotes phagocytosis when disrupted (Supplementary Fig. 1g). In addition to known factors, unexpected hits involved in lipid metabolism, sialic acid biosynthesis, and the poorly characterized genes *NHLRC2, TM2D1, TM2D2,* and *TM2D3* represent some of the strongest genetic regulators of phagocytosis in this system, with either general or selective effects on particle uptake (Supplementary Fig. 1g).

Multiple genome-wide screens for diverse particle types reveal universal and substrate-specific hits

To allow for magnetic selection of cells based on phagocytosis of additional substrates, we covalently conjugated 30 nm diameter iron oxide nanoparticles (lONPs) to purified myelin, zymosan (yeast cell wall particles) and sheep red blood cells (RBCs) conjugated with either IgG (IgGRBC) or complement (CompRBC). We also sought to more directly address the function of particle size and charge in phagocytosis. To this end, we performed additional genome-wide screens using superparamagnetic beads of 0.43 μm diameter (SmallBeads), 4.3 μm diameter (BigBeads), as well as oppositely charged, cationic 1.3 μm diameter beads (PosBeads) (Fig.1a). Magnetic labeling and phagocytosis of each substrate was optimized for efficient separation of phagocytosing U937 cells (Fig 1f, Supplementary Figs. 2a–j, Supplementary Table 3, Supplementary Text). We conducted genome-wide phagocytosis screens for all eight substrates, each in duplicate. Screen hits were typically moderately to highly expressed by both differentiated U937s and primary human microglia (Supplementary Fig. 3a, Supplementary Table 4); this suggests our approach identifies genes relevant for phagocytosis in U937 and primary macrophages.

To compare the highest-confidence phagocytosis regulators across all eight screens, we compiled a subset of 150 genes containing genes recovered at FDR 5% in at least two independent substrate screens. Unbiased hierarchical clustering revealed distinct categories of genes whose deletion either promotes or inhibits phagocytosis for all substrate types, or which have differential contributions for different types of substrates. In general, genes known to participate in the same process clustered together (Fig 1g).

We manually binned genes recovered at FDR 5% in at least three genome-wide screens into functional categories based on their reported roles within the cell (Fig. 2). Among the highest-confidence hits are the aforementioned members of the SCAR/WAVE and ARP2/3 complexes, all ten non-redundant members of which were hits for almost every substrate screened. The ARP2/3 complex was recently shown to be of limited importance for IgG-mediated phagocytosis[40], and ARP2/3 components showed the lowest signal in IgGRBC screens (Fig. 2). Among the most prominent negative regulators of phagocytosis were 7 genes associated with sialic acid biosynthesis and protein sialylation (Fig. 2). Genes related to surface signaling (such as the integrin associated genes *ITGB2, TLN1,* and *FERMT3*) and intracellular kinase/phosphatase cascades (such as PP2A, MAPK, and PKC-related genes) were among the hits with the strongest differential impact across different substrates.

Large-scale orthogonal validation of phagocytosis hits by FACS and automated microscopy

Our novel magnet-based phagocytosis screens yielded hundreds of hits, however we considered that some hits could result from properties unique to the magnetic separation process. To confirm that genes identified in these genome-wide screens are indeed related to phagocytosis, we performed an orthogonal FACS-based validation screen in which phagocytosis can be monitored by the pH-sensitive fluorescent dye, pHrodo (Fig. 3a). To do this, we generated a smaller sub-library comprised of sgRNAs targeting 322 genes identified as hits in the first BigBead and CompRBC genome-wide screens (Supplementary Tables 5

and 6). The reduced scale of the sub-library enabled rapid FACS-based selection of 3×10^6 cells (~900x coverage). There was general agreement between the effect of sgRNAs in the FACS based screen and the magnetic screens ($R^2 = .4$) (Fig. 3b), confirming that screen hits are not limited to idiosyncrasies of the magnetic selection method.

To further refine a highly confident set of differential hits across diverse substrates, we again leveraged the advantages of our magnetic separation approach to screen the small sub-library using six substrates at much higher coverage than the genome-wide screens (60,000 cells per unique guide vs 1,000 cells per unique guide). This increased coverage, as determined by the number of cells per unique guide, has been previously shown to improve sensitivity and robustness of large-scale screens[33,41]. In particular, we noted that for certain substrates the genome-wide screens exhibited low signal and high noise (Supplementary Fig. 3b), possibly due to the single magnetic separation step or heterogeneous differentiation and phagocytosis in U937 cells. While the false discovery rate can be controlled with stringent filtering, this may result in a high number of false negatives, i.e. genes that effect phagocytosis but do not reach significance due to noise and/or small effect sizes. As expected, the high-coverage sub-library screens showed higher reproducibility between replicate screens (Supplementary Fig. 3c) and general agreement with genome-wide screens (Supplementary Figs. 4a,b), though certain screens did show a number of apparent false positive results. The batch retest screens revealed phenotypes for many genes that had been missed in the genome-wide screens (false negatives). Additionally, we created a library targeting the 218 mouse genes whose human orthologues showed strong effects in the genome-wide midbead screen and screened it using FACS based separation in one of the most widely studied phagocytic cell lines, mouse RAW 264.7 cells. While this cross-species comparison in a different cell line revealed many genes that appear to have species-specific or cell-type specific effects on phagocytosis, 81 of the genes in this library still demonstrated a significant phagocytosis phenotype (Supplementary Fig. 4b, Supplementary Table 5). Together, these focused, high-coverage sub-library screens largely confirmed hits identified in genome-wide screens, and further supported the findings of strong effects for several poorly characterized genes (Supplementary Table 5).

Additionally, we generated 34 stable U937 cell lines expressing Cas9 and individual sgRNAs targeting hits identified at 10% FDR in our genome-wide screens, and confirmed high rates of gene editing (Supplementary Fig. 4g). We then measured rates of phagocytosis using automated time-lapse microscopy of pHrodo-labeled substrate. For example, differentiated U937 cells expressing sgRNAs against the SCAR/WAVE complex member *NCKAP1L* exhibited dramatically reduced phagocytosis (Figs. 3c, d). These orthogonal time-lapse microscopy validation assays demonstrated varying degrees of reduced or increased phagocytic capacity across multiple substrates which largely mirrored the original screen results (Fig. 3e, Supplementary Fig. 4c,d, Supplementary Table 7) and validated contributions of genes with no previously reported role in phagocytosis (Fig. 3e). Together, ~70–80% of genes (depending on substrate) measured in these individual assays exhibited a phenotype consistent with their phenotype in the pooled screens. Finally, we validated the roles of select genes by CRISPR editing in primary human macrophages isolated from peripheral blood, suggesting that hits discovered in these screens are not limited to immortalized cell lines (Fig. 3f,5e,6f, Supplementary Fig. 4i).

Identification of substrate-selective regulators of phagocytosis

Intriguingly, the screens revealed several genes whose disruption had a differential impact on phagocytosis for certain substrates. To directly test the effect of these genes on substrate preference, we adapted our live-imaging phagocytosis assay to simultaneously monitor uptake of two separate particles labeled with pHrodo-red and pHrodo-green respectively (Fig. 3g). Using this approach, we challenged several sgRNA expressing U937 lines either with a mixture of red zymosan and green positive midbeads or with a mixture of red CompRBC and green positive midbeads. Consistent with the screen results, U937 cells expressing sgRNAs against integrin-related genes *TLN1* and *FERMT3* showed dramatic reduction in phagocytosis of zymosan and CompRBC, while their ability to phagocytose beads remained intact (Figs. 3h–j). Additionally, we confirmed that *PLEK,* which has previously been implicated in coordinating actin polymerization and has been reported to be enriched at the phagocytic cup[42,43], also contributes to uptake of the zymosan and complement opsonized red blood cells, but not beads (Figs 3h–j).

Multiple magnetic screens predicted that knockout of *PLEK, TLN1, ICAM1,* and *CDK2* would boost bead phagocytosis. Interestingly, while cell lines expressing *CDK2* sgRNAs similarly increased uptake of beads measured using pHrodo-labeled beads (which measure pH drop upon phagosome fusion to the lysosome) (Supplementary Fig. 4d), we saw no increase phagocytosis in pHrodo-based assays for *ICAM1, PLEK, TLN1* knockouts (Fig 3h–j, Supplementary Fig. 4d). To investigate this discrepancy, we tested cells carrying sgRNAs for PLEK or TLN1 in magnetic separation assays after exposure to magnetized zymosan or magnetic beads. Indeed, these assays again confirmed deficits in zymosan uptake for these lines and showed increased capture of bead-exposed cells (Supplementary Fig. 4f). U937 cells carrying *ICAM1* sgRNAs similarly showed no effect in pHrodo-based assays, but showed increased magnetic capture after phagocytosis of magnetic beads or zymosan (Supplementary Fig. 4e). Thus, while the assays largely correlate well (Fig. 3b), certain phagocytosis regulators we identified showed selective effects in magnetic bead uptake vs. pHrodo bead uptake assays, which could reflect action at distinct steps of phagocytosis. This underscores the value of using orthogonal assays to probe the activity of identified phagocytosis regulators.

Discovery of an essential role for NHLRC2 in phagocytosis

A particularly conspicuous hit from our screening datasets was *NHLRC2,* a poorly characterized gene that was reproducibly one of the strongest hits required for phagocytosis in almost every screen. To further validate the role of NHLRC2 during phagocytosis, we examined its function in RAW 264.7 cells. RAW 264.7 cell lines were generated constitutively expressing Cas9 and an sgRNA targeting either *NHLRC2* or the SCAR/WAVE component *NCKAP1L.* We observed almost identically strong defects in phagocytosis for two independent sgRNAs targeting each of these genes (Supplementary Fig. 5a). In order to further validate this observation, we generated clonal *NHLRC2* knockout RAW 264.7 and U937 cells, confirmed by Sanger sequencing (Supplementary Fig. 4h), and found severe phagocytosis deficits. (Figs. 4a, b Supplementary Fig. 5b). In addition, we validated the inhibitory of effect on phagocytosis when knocking out these genes in primary human macrophages (Fig 3f).

To investigate the molecular function of NHLRC2, we performed BioID pulldown experiments[44] using a BirA*-NHLRC2 fusion protein. This approach allows for the unbiased assessment of transient or stable NHLRC2 interactions within the native cellular environment of differentiated U937s. BirA*-NHLRC2 pulldown samples were highly enriched for several transmembrane and peri-membrane proteins in addition to NHLRC2 itself (Fig. 4c, Supplementary Table 8). Surprisingly, none of the partners were identified as a hit in any of our phagocytosis screens, possibly due to redundancy of NHLRC2-associated proteins (see Discussion). However, gene ontology and KEGG enrichment analysis of pulldown hit genes identified enrichment in annotated phagocytosis regulators (Supplementary Table 8), with two candidates (LSP1 and p190RhoGAP) directly implicated in directing actin polymerization at the cell surface[45,46]. Therefore, we hypothesized that *NHLRC2* contributes to phagocytosis by assisting LSP1 or p190RhoGAP coordination of actin polymerization.

p190RhoGAP (also known as GRLF1 or ARHGAP35) is a negative regulator of RHOA and has been shown to localize to the phagocytic cup[47]. RHOA influences bundled actin dynamics and antagonizes Rac1-mediated rearrangements of branched cortical actin. We therefore tested whether loss of *Nhlrc2* alters RHOA or RAC1 activation. *Nhlrc2* knockout RAW 264.7 cells showed substantially elevated levels of RHOA activation specifically during phagocytosis, although global levels of RAC1 activation were minimally altered in total cell lysates (Fig. 4d, Supplementary Fig. 5c). We next tested whether enhanced Rac1 activity could overcome *Nhlrc2* knockout phagocytic deficits by overexpressing a constitutively active Rac1 mutant (RAC1Q61L). RAC1Q61L overexpression rescued the phagocytic defect of *Nhlrc2* knockout cells without impacting control or *Nckap1l* knockout cells, supporting a model in which NHLRC2 is required for cytoskeletal rearrangements downstream of particle binding and receptor engagement (Fig. 4e). Closer examination of cellular morphology by scanning electron microscopy revealed a striking loss of surface filopodia specific to *Nhlrc2* knockout cells relative to wild-type or *Nckap1l* knockout cells (Fig. 4f, Supplementary Fig. 5e), supporting a role for NHLRC2 in regulation of actin protrusions. The absence of filopodia in *Nhlrc2* knockout cells was also observed using confocal microscopy following phalloidin staining to label F-actin (Fig. 4g, Supplementary Fig. 5d) as well as failure to form organized actin structures in a frustrated phagocytosis assay (Fig. 4h, Supplementary videos 1,2). Together, these data suggest a model in which NHLRC2 negatively regulates RHOA, enabling RAC1-mediated cytoskeletal changes that are critical for phagocytosis (Fig. 4i).

Very long chain fatty acids (VLCFAs) are necessary for efficient phagocytosis

Among unexpected hits were members of a sequential lipid biosynthesis pathway (Fig. 5a). These included a fatty-acid elongase that generates VLCFAs (*ELOVL1*), and a ceramide synthase that specifically incorporates VLCFAs into ceramides (*CERS2*), which were strong hits for multiple substrates (Fig. 1g). A downstream sphingomyelin synthase that adds a zwitterionic head group to a diverse range of ceramides (*SGMS1*)[48] was also hit, though with weaker and more variable effects. In validation experiments, sgRNAs targeting any of these three enzymes strongly reduced phagocytosis of zymosan (Fig. 5b). To test whether the contribution of these genes to phagocytosis is solely related to the presence of these lipid

species, we performed metabolic rescue experiments. Phagocytosis deficiency of cells with disrupted *ELOVL1* function could be rescued by supplementation with its product VLCFAs (a mixture of C24:0 and C24:1), but not its substrate medium-chain fatty acids (a mixture of C18:0 and C18:1, Figs. 5 c,d). Importantly, control cells were not affected and cells carrying an sgRNA against the downstream enzyme *CERS2* were not rescued. We further validated the role of *ELOVL1* in phagocytosis by CRISPR editing in primary human macrophages; despite incomplete gene editing (Supplementary Fig. 4i), we observed a significant decrease in phagocytosis in upon *ELOVL1* gene disruption (Fig. 5e).

Interestingly, confocal microscopy of *ELOVL1* KO RAW 264.7 cells incubated with IgG coated 7 μM beads and fixed after 10 minutes indicated a majority of phagocytic cups are stalled at early cup formation. By contrast, all steps of phagocytic cup formation, including fully engulfed beads, could be observed in control cells (Fig 5f, Supplementary Fig. 6a, Supplementary videos 3,4). The phenotype of early phagocytic cup stalling in *ELOVL1* KO cells was also observed by scanning electron microscopy (Fig. 5g, Supplementary Fig. 6b).

Since the process of cell migration involves similar actin dynamics and many of the same molecular components as phagocytosis, we tested whether VLCFAs might play a role in migration. Interestingly, knockdown of *ELOVL1* in a human neutrophil cell line (PLB-985) reduced basal cell migration speed, although not as strongly as positive control genes (*ACTR2* and *RAC2,* previously shown to have roles in both phagocytosis and cell motility[49] (Supplementary Fig. 6c). This motility defect was reduced after stimulation with a formyl peptide chemoattractant (Supplementary Fig. 6d). For the two sgRNAs we tested, the strength of the knockdown correlated with the strength of the phenotype (Supplementary Fig. 6c–e). Taken together our results suggest a previously unappreciated role of these specific VLCFAs in basic immune cell functions requiring large morphological transitions such as macrophage phagocytosis and neutrophil motility.

Examination of substrate-specific regulators reveals an Aβ–specific phagocytic defect in TM2D3, an uncharacterized Alzheimer's-associated gene

In addition to integrin-related genes identified as specifically impacting uptake of a subset of particles (Supplementary Fig. 7a, b), we chose to focus on the TM2D family (*TM2D1, TM2D2,* and *TM2D3*), several components of which were consistently recovered as hits required for phagocytosis for various beads types but were either not hits or had weak effects on uptake of most biological particles (Fig. 1g, Fig. 2).

TM2D1 has been previously implicated in binding to amyloid-beta peptide[50], and a *TM2D3* variant allele was recently identified as strong risk factor for late-onset Alzheimer's disease, with an odds-ratio of 3.5–15.9[51]. Therefore, we hypothesized that TM2D family members participate in engulfment of amyloid-β (Aβ) protein aggregates. To test this, we generated small pHrodo-conjugated Aβ aggregates according to previously described protocols[52]. Control cells showed actin-dependent accumulation of pHrodo signal, and uptake was abolished with the addition of cytochalasin D (Supplementary Fig. 7c). Uptake of pHrodo-conjugated Aβ aggregates was also dramatically reduced in U937 cells with sgRNAs targeting universally required phagocytosis regulators, such as *NCKAP1L* and *NHLRC2* (Supplementary Fig. 7c). Because phagocytosis of Aβ aggregates and synaptic material are

both thought to be important for Alzheimer's disease progression[4] and our screens predicted strong substrate-specific contributions of TM2D family members, we next tested whether knockout lines could discriminate between simultaneously-applied pHrodo-red Aβ and pHrodo-green synaptosomes. *TM2D2* and *TM2D3* knockout lines showed substantial deficiencies in Aβ phagocytosis, but less of a change in clearance of synaptic material in a competition assay (Figs. 6 a–c), highlighting the potential significance of CNS substrate-specific contributions of TM2D family proteins to the balance of phagocytosis in Alzheimer's disease. To further confirm the role of TM2D family proteins, we tested the role of *TM2D3* in the phagocytosis of Aβ aggregates and zymosan in primary human macrophages. We observed that *TM2D3* RNPs inhibited the phagocytosis of Aβ aggregates by peripheral blood monocyte derived macrophages while no change was detected for zymosan phagocytosis. (Figure 6d). Together, these data suggest that loss of *TM2D3* function may impair clearance of Aβ aggregates and related particles, with more limited impact on phagocytosis of other substrates.

Discussion

Here, we develop a rapid and efficient strategy to identify genes that control diverse aspects of phagocytosis using magnetic separation. We have implicated many known and uncharacterized genes as positive or negative regulators of phagocytosis, and validated the roles of dozens of individual genes using orthogonal assays. Together, our data illuminate both universal and substrate-specific principles of phagocytosis and identify multiple novel and poorly characterized genes that are central to phagocytic processes.

Identification of NHLRC2 as a potent regulator of phagocytosis and filopodia formation

NHLRC2, one of the strongest hits across almost all of our screens, has been poorly characterized but is broadly expressed at relatively low levels in many cell types[53]. During preparation of this manuscript, mutations in *NHLRC2* were found to be associated with fatal fibrosis, CNS vascular abnormalities, and neurodegeneration in humans[54], and a role was proposed for *NHLRC2* in protection from ROS-induced cell death[55]. Our results show that knockout of *NHLRC2* in U937 and RAW 264.7 cells profoundly inhibits phagocytosis of several types of substrates. Rescue of murine *Nhlrc2* knockout cells with constitutively active Rac1 suggests that phagocytic signaling can be restored and that cells lacking NHLRC2 protein are otherwise capable of executing the steps required for phagocytosis. With the additional observation that NHLRC2 associates with p190RhoGAP and alters activation levels of the cytoskeleton regulator RHOA, we propose a model in which NHLRC2 helps to initiate localized RHOA inhibition, enabling RAC1-driven cytoskeletal rearrangement during initiation of phagocytosis. The mechanism by which loss of NHLRC2 results in loss of filopodia (Fig. 4f,g) will require further investigation, but may partially explain the profound defect in phagocytosis observed in these mutant cells[56].

Identification of substrate-specific regulators of phagocytosis

We find clusters of genes with differential effects on distinct substrates (Fig. 1g, Fig. 2); for example, integrin signaling is required for uptake of several biological particles but not charged beads (Fig. 1g, Fig. 2). Integrins can act as phagocytic receptors themselves, but

also serve to facilitate initiation of phagocytic signaling cascades after engagement of other surface receptors. Additionally, we found that PLEK, which serves to localize and initiate signaling cascades that direct cytoskeletal rearrangements and can be localized to the phagocytic cup[42,43], plays a role only upon engagement of certain substrates. Conversely, many genes regulate phagocytosis of beads but not biological particles (Fig. 1g). Further studies will be necessary to investigate the mechanisms which account for these differences.

Discovery of role for TM2D family proteins in Aβ uptake

In considering hits with disproportionate impacts on different particle types, we were particularly intrigued by the TM2 domain family members because they are poorly characterized and have been implicated in neurodegenerative disease. We found that *TM2D2* and *TM2D3* deficient cells show impaired clearance of Aβ aggregates, and that the phagocytic defect had a disproportionate effect on protein aggregates relative to another CNS-relevant substrate. Previous findings that TM2D1 can directly bind to Aβ peptide[50] suggests that these genes may contribute to initial events required for aggregate uptake. However, all three TM2 domain family members are broadly expressed by diverse cell types[53], and they may play a more general role in cellular signaling events related to disease progression.

The ability to rapidly screen for phagocytosis regulators at genome scale opens the possibility of investigating how phagocytosis machinery changes across cellular activation states or in diverse environmental conditions. Further optimization can address limitations of this approach and should allow more detailed dissection of particular steps of phagocytic particle engulfment (see Supplementary Text). Together, this work establishes a broadly applicable strategy for investigating complex cellular uptake processes and promises to yield critical insights into diseases characterized by dysregulated phagocytosis.

Online Methods

U937 cell culture and differentiation—U937 cells were acquired from ATCC (CRL-1593.2). Cells were maintained in suspension culture using spinner flasks for library propagation and tissue culture plates for single-gene knockout lines, all in sterile- filtered U937 growth medium (RPMI1640 supplemented with 2 mM glutamine, 100 units/mL penicillin, 100 mg/mL streptomycin, and 10% heat-inactivated fetal calf serum). Cells were cultured in a humidified 37°C incubator set at 5% CO_2. Cells were passaged 2–3 times weekly. To generate frozen aliquots, cells were pelleted by centrifugation (300g, 7 min, room temperature), suspended in 90% FCS/10% DMSO, and frozen in cell freezing containers at −80°C overnight before transfer to liquid nitrogen for long-term storage.

For differentiation, U937 cells were diluted to a density of 1–2 million cells per mL in U937 growth medium containing phorbol myristate acetate (PMA) to achieve a final concentration of 50 nM PMA. Cells were plated on tissue culture plastic and allowed to differentiate and adhere for 3 days. After differentiation, cells were recovered by harvesting supernatants and trypsinizing adherent cells. For trypsinization, cells were washed three times with phosphate buffered saline (PBS; 137 mM NaCl, 2.7 mM KCl, 8 mM sodium phosphate dibasic, 2 mM potassium phosphate monobasic, pH 7.4), incubated in PBS containing 300 units/mL trypsin

for 7 min at 37°C, then recovered from the plate by repeatedly pipetting the solution to dislodge cells. Trypsinized adherent and non-adherent supernatant cells were pooled, pelleted by centrifugation (300g, 7 min, room temperature), and resuspended in fresh U937 growth medium. Cells were then plated and allowed to recover for two days before performing assays. For screens, 100 million differentiated U937 cells were plated in 100 mL of U937 growth medium in 15 cm tissue culture dishes. For validation assays and other experiments, cells were plated at a density of 500,000 cells/mL in 96-well plates.

CD11b Staining—U937 cells were differentiated in 50nM PMA as described above or left undifferentiated and 500,000 cells per well were plated in a glass bottom 24-well plate. On day five post-differentiation cells were washed 2x with cold dPBS, blocked with 500ul 3%BSA in dPBS for 1 hr, then incubated for 30 min with 500ul of a 1:200 dilution of the CD11b antibody (Biolegend - Cat # 101202, Clone M1/70). Cells were then washed 3x with cold dPBS. Secondary antibody (donkey anti-rat AlexaFluor 488, Thermo Fisher – Cat #: A-21208) was added at a 1:1000 dilution in dPBS and incubated in the dark for 1 hour. Cells were then washed 5x in cold dPBS. Cells were then incubated with a 1:10,000 dilution of Hoescht for 3 min in the dark and washed 1x with cold dPBS.

RAW 264.7 cell culture—RAW 264.7 cells were acquired from ATCC (TIB-71). Cells were maintained on tissue culture plastic in RAW growth medium (DMEM supplemented with 2 mM glutamine, 100 units/mL penicillin, 100 mg/mL streptomycin, and 10% heat-inactivated fetal calf serum). Cells were passaged by gently lifting the cells with a disposable cell scraper, pelleting by centrifugation (300g, 7 min, room temperature), and replating the cells in fresh RAW growth medium.

Library preparation—The 10-sgRNA-per-gene CRISPR/Cas9 deletion library was synthesized, cloned, and infected into Cas9 expressing U937 cells as previously described (Morgens et al., 2017). Briefly ~300 million U937 cells stably expressing SFFV-Cas9-BFP were infected with the 10 guide per gene genome-wide sgRNA library at an MOI < 1. Infected cells underwent puromycin selection (1 μg/mL) for 5 days after which point puromycin was removed and cells were resuspended in normal growth medium without puromycin. After selection sgRNA infection was measured as >90% of cells as indicated measuring mCherry positive cells by flow-cytometry. Sufficient sgRNA library representation was confirmed by deep sequencing after selection. Selected library-carrying U937 cells were stored in liquid nitrogen, and cells were thawed and expanded for at least 5 days before differentiation for screens.

Generation of individual sgRNA expressing U937 and RAW 264.7 cell lines

For generating individual sgRNA phenotypes we lentivirally infected U937 cells stably expressing SFFV-Cas9-BFP or RAW 264.7 cells stably expressing EF1Alpha-Cas9-BFP with constructs expressing a given sgRNA along with puromycin resistance. Three days after infection we selected with (1 μg/mL) puromycin for U937s and (10 μg/mL) for RAW 264.7 cells for five days. In cases where single cell clonal knockout lines were derived, after puromycin selection single cells were sorted into 96-well plates and expanded for two to three weeks.

Gene editing measurements by sanger sequencing

Cells were harvested and total genomic DNA was isolated using QuickExtract DNA Extraction Solution (VWR, Radnor, PA, cat# QE09050). PCR was prepared using 5X GoTaq Green Reaction Buffer and GoTaq DNA Polymerase (Promega, Madison, WI, cat# M3005), 10 mM dNTPs, and primers designed approximately 250–350 basepairs upstream and 450–600 basepairs downstream of the predicted cut site. PCR reactions were run on a C1000 Touch Thermo Cycler (Bio-Rad). PCR products were then purified over an Econospin DNA column (Epoch, Missouri City, TX, cat# 1910–250) using Buffers PB and PE (Qiagen, Hilden, Germany, cat# 19066 and cat# 19065). Sanger sequencing ab1 data were obtained from Quintara Biosciences and editing efficiency of knockout cell lines were analyzed using Synthego's online ICE Analysis Tool.

Phagocytosis substrate preparation

Details for all phagocytosis substrates, IONP labeling reactions, and pHrodo labeling reactions can be found in Supplementary Table 3. Midbeads, SmallBeads, Bigbeads, and Posbeads (Spherotech) were stored at 4°C and pelleted then resuspended in PBS prior to use. Zymosan (Sigma) was suspended to 10 mg/mL in PBS then filtered through a 40 μm cell strainer (BD Biosciences) to remove large poorly-resuspended material. Myelin was prepared using perfused total brain homogenate from adult rats following a published protocol [57]. Myelin concentration was estimated using wet pellet weight, and myelin was stored in single-thaw aliquots of 20–100 mg/mL at −30°C. Sheep erythrocytes (RBCs, MP Biomedicals) were opsonized following a published protocol[58] prior to conjugation of IONPs or pHrodo. Briefly, cells were washed with PBS, incubated with polyclonal rabbit anti-sheep RBC IgG or polyclonal rabbit anti-sheep RBC IgM followed by complement factor 5 depleted serum (C5d serum), and then washed repeatedly before storage at 4°C in dPBS with calcium and magnesium for up to 4 weeks. For unopsonized, IgM opsonized, or C5d serum opsonized RBCs, all wash and incubation steps were performed as for complement opsonized cells except IgM and/or C5d serum, were omitted as appropriate.

Synaptosomes were prepared using perfused whole brain from adult rats based on density centrifugation according to a published protocol[59] and stored at −30°C in single-thaw aliquots.

Amyloid β (Aβ) aggregates were generated according to a published protocol [52] by dissolving human beta amyloid (1–42) (Anaspec) in hexafluoroisopropanol, drying, re-dissolving in DMSO, diluting to 200 mM in PBS, and incubating the peptide for 24 hr at 4°C to promote formation of oligomeric Amyloid p aggregates. Aβ aggregates were labeled with pHrodo by adding pHrodo Red succinimidyl ester to 200 μM and incubating at room temperature for 30 min protected from light on a rocker, after which unconjugated pHrodo dye was separated using size-exclusion Bio-Gel P-6 spin columns prewashed in screening media (Bio-Rad). Aβ aggregates were stored at 4°C and used within 24 hours of aggregation. Aβ was added at a concentration of 15 mM for phagocytosis assays.

IONP and pHrodo conjugation to phagocytosis substrates

Phagocytosis substrates were covalently labeled at free amine groups with 30 nm diameter iron oxide nanoparticles (lONPs) with N-succinimidyl ester functionalization (Sigma), with pHrodo Red succinimidyl ester (ThermoFisher Scientific), or with pHrodo Green STP ester (ThermoFisher Scientific). Except for Aβ, substrates were pelleted by centrifugation, resuspended in PBS to a fixed concentration, and incubated with a set amount of pHrodo or IONP for 45 minutes at room temperature with gentle shaking. Centrifugation time, substrate concentration, and label concentration varied with each substrate as described in Supplementary Table 3 in order to optimize particle integrity, prevent particle clumping, and maximize sensitivity of downstream assays. Supernatants of the final wash did not have detectable levels of fluorescence from free pHrodo dye, and did not result in pHrodo+ puncta when incubated with phagocytic cells. After magnet or pHrodo conjugation, phagocytosis substrates were stored in PBS at 4°C for less than 1 week (IONP conjugation) or less than 1 month (pHrodo conjugation). RBCs were washed twice immediately before use to remove any lysed cells and minimize risk of heme inhibition of phagocytosis.

MidBeads, SmallBeads, and BigBeads lack inherent free amine reactive groups, and so were sparsely conjugated with putrescine via EDC (1-ethyl-3-(3-dimethylaminopropyl)carbodiimide hydrochloride, ThermoFisher Scientific) crosslinking prior to addition of pHrodo. Beads were washed twice in PBS pH 5.5 (PBS adjusted to pH 5.5 with HCl) and resuspended to 5% w/v in PBS pH 5.5. The bead suspension was mixed 1 to 1 with a 1M putrescine solution before addition of freshly-dissolved EDC crosslinker to 1 mg/mL. Beads were incubated 2hr at room temperature before washing three times in PBS (neutral pH) and resuspension for pHrodo conjugation. The EDC concentration was titrated to prevent bead crosslinking and to incorporate the minimal amount of amine groups that allowed for efficient detection of pHrodo signal at pH 5.5 after subsequent bead labeling.

Magnetic-separation based CRISPR screens

U937 cells carrying sgRNA library were differentiated with 50 nM PMA for 3 days, trypsinized, and replated at 100 million cells per 15 cm dish as described above. After 2 days of recovery in growth medium lacking PMA, cells were washed 8 times with dPBS with calcium and magnesium (dPBS+, Gibco). Cell medium was exchanged to 15 mL of serum-free U937 growth medium (U937 growth medium lacking FCS) and returned to the incubator for 5 min. Then, 5 mL of pre-warmed serum-free U937 growth medium was added containing phagocytosis substrate at the concentrations described in Supplementary Table 3. Cells were returned to the incubator for a fixed amount of time depending on the prey, as described in Supplementary Table 3.

After phagocytosis, dishes were rinsed 10 times with dPBS+ to remove uningested particles. For screens involving RBCs, dishes were exchanged into ACK lysis buffer and swirled for 10 seconds to promote RBC lysis prior to dPBS+ washes. Cells were then exchanged into 15 mL of Medium A and 100 uL of trypsin stock solution (30,000 units per mL stock, Sigma) was added to each plate. Cells were returned to the incubator for 10 min to facilitate cell removal from the culture dish and substrate removal from the cell surface. After trypsinization, 3 mL of Medium A containing 10 mM MgCl2 was added to each dish to

minimize cell lysis and bead aggregation. 40 uL of DNase I stock solution (0.4% DNase, Worthington) was added to each plate to prevent carryover of gDNA from lysed cells.

Cells were dislodged from the dish with repeated pipetting and passed through a 40 μm cell strainer (BD Biosciences) to remove aggregated cells. Cells were subsequently agitated periodically to minimize cell settling and potential aggregation. To maximize cell recovery, 12 mL of separation buffer (12 mL of Medium A with 2 mM MgCl2 and 0.1% Milk peptone (Sigma)) with 0.001% DNAse I was added to each dish and remaining cells were recovered with a cell scraper. Scraped cells were pipetted repeatedly, passed through a 40 μm cell strainer (BD Biosciences), and combined with pipetted cells.

Next, cells were passed over 4–6 LS magnetic columns (Miltenyi) equilibrated with separation buffer and mounted in the magnetic holder. Only 2 mL of cell suspension was applied to each column at a time, and was allowed to drain before immediately adding an additional 2 mL of cell suspension. Column flowthrough was collected and reserved as the unbound fraction. After all of the cell suspension had been loaded, columns were washed three times with 2 mL of separation buffer and flowthrough was combined with the unbound fraction. After 3 washes, columns were removed from the magnetic apparatus and 3 mL of separation buffer was gently flushed through the demagnetized column with a syringe plunger. The column eluate was reserved as the bound fraction. EDTA was added to achieve a final concentration of 2 mM to each fraction and cells were pelleted by centrifugation (7 min at 300g, room temperature). Cells were resuspended in 90% FCS/10% DMSO with 2 mM EDTA and frozen in cell freezing containers at −80°C for subsequent genomic DNA extraction.

For pilot experiments and to determine the phagocytosis duration required to capture the majority of U937 cells on the magnet, the above experiments were scaled-down to 6-well plated. For cytochalasin D experiments, cytochalasin D was added to 10 μM 5 min before addition of phagocytosis substrate. After recovery of the bound and unbound fractions, cells were resuspended in dPBS+ containing 1.33 μM Calcein AM (Invitrogen) to visualize live cells.

Screen analysis

At the end of each screen genomic DNA was extracted for all screen populations separately according to the protocol included with QIAGEN Blood Maxi Kit. Using known universal sequences present in the lentivirally-incorporated DNA, sgRNA sequences were amplified and prepared for sequencing by two sequential PCR reaction as previously described (Morgens et al., 2016). Products were sequenced using an Illumina Nextseq to monitor library composition (30 to 40 million reads per library). Trimmed sequences were aligned to libraries using Bowtie, with zero mismatches tolerated and all alignments from multi-mapped reads included.

Guide composition and comparisons across bound and unbound fractions was analyzed using casTLE (Morgens et al., 2016) version 1.0. Briefly, for each pair of bound and flow-through samples, guides with fewer than 25 counts in both conditions were removed from the analysis. If a guide had fewer than 25 counts in a single condition, this value was

changed to be equal to 25 counts. Enrichment of individual sgRNAs was then calculated as a median-normalized log-ratio of the fraction of counts, as previously described[60]. For each gene, a maximum likelihood estimator was used to identify the most likely effect size and associated log-likelihood ratio (confidence score) by comparing the distribution of gene-targeting guides to a background of nontargeting and safe-targeting guides. P-values were then estimated by permuting gene-targeting guides, and hits were called using FDR thresholds (Supplementary Table 1) calculated via Benjamini-Hochberg. For small-scale retest and FACS screens, a similar analysis was used except genes were called as hits when their effect score at 95% credible interval did not include zero[61,62] (Supplementary Table 5). Additionally, for small-scale magnetic screens, a count threshold of 100 was used to adjust for higher sequencing coverage. Permutations were not used to calculate p-values for small-scale retest screens as a large fraction of guides in these screens are expected to have effects on phagocytosis. Two more stringent analyses were also included: (1) requiring genes to pass the 95% credible interval in both individual replicates, and (2) analysis of the small-scale retest screening using MAGeCK[63] (Supplementary Table 5). MAGeCK (version 0.5.6) was run using the 'mageck test' command supplied with the '--norm-method control' option and otherwise default options.

pHrodo phagocytosis assay

U937 cells were differentiated as above for magnetic separation. After 3 days of PMA exposure, cells were lifted, centrifuged, and re-plated in 96-well tissue culture plates at a density of 50,000 cells per well in 100 μL U937 growth medium. After 2 additional days of recovery, non-adherent cells were eliminated by washing twice with dPBS. Then, dPBS was removed and replaced with pre-warmed serum-free U937 growth medium (U937 growth medium lacking 10% FBS) containing the appropriate pHrodo-labeled phagocytosis substrate(s) at the concentration denoted in Supplementary Table 3.

Some experiments included Cytochalasin D (10 μM) in the serum-free U937 growth medium for select wells. For fatty acid rescue experiments (Figure 5), fatty acids (Cayman Chemical) were added first to U937 growth medium used when cells were plated in 96-well plates, and second to serum-free U937 growth medium containing phagocytosis substrates (C18s: stearic acid and oleic acid at 3 μg/mL each or lignoceric acid and nervonic acid 3 μg/mL each, all from ethanol stocks). All cell plating in 96-well plates, washing, and addition of phagocytosis substrates were performed using a multichannel pipette.

After addition of phagocytosis substrates, cells were returned to the incubator and imaged at 30 to 60 min intervals using an Incucyte (Essen). The first time point (reported as t = 0) was typically acquired within 5–20 min of cells returning to the incubator. Reported values are averaged over four fields per well, with at least 4 wells used per data point. Images were acquired with at 20x objective at 400 ms (green) or 800 ms (red) exposures per field. After the last imaging time point, calcein-AM (Invitrogen) was added to a final concentration of 1.33 μM. Cells were incubated with calcein-AM for 15 min before a final image acquisition to determine total live cell area per field. No visual decrement in cell survival or health was noticeable after 24 hours of imaging in serum-free medium.

To calculate a phagocytic index for each well, the total pHrodo-positive area was determined for each time point and normalized to the total calcein-positive live cell area measured immediately after the 5 hour time point. Total area was calculated using automated analysis scripts that performed a fixed-value adaptive background subtraction and selected signal-positive regions that passed intensity thresholds. Different analysis scripts were generated for each phagocytosis substrate to accurately report signal from ingested material. Cellular localization and accurate selection of pHrodo or calcein signal was confirmed visually.

For phagocytosis assays with RAW 264.7 cells, cells were plated at 25,000 cells per well of a 96- well plate. One day later, cells were washed twice with dPBS and exchanged into serum-free RAW cell growth medium. For cells transduced with constitutively active Rac1, Rac1 expression was induced by addition of 5 ng/mL doxycycline at the time of transfer to 96-well plates and doxycycline was removed upon transfer to serum-free medium for phagocytosis assays. RAW 264.7 cell phagocytosis was imaged and analyzed as for U937 cells.

Supplementary Material

Refer to Web version on PubMed Central for supplementary material.

ACKNOWLEDGEMENTS

References:

1. Lim JJ, Grinstein S & Roth Z Diversity and Versatility of Phagocytosis: Roles in Innate Immunity, Tissue Remodeling, and Homeostasis. Front Cell Infect Microbiol 7, 191, doi:10.3389/fcimb. 2017.00191 (2017). [PubMed: 28589095]

2. Gordon S Phagocytosis: An Immunobiologic Process. Immunity 44, 463–475, doi:10.1016/ j.immuni.2016.02.026 (2016). [PubMed: 26982354]

3. Arandjelovic S & Ravichandran KS Phagocytosis of apoptotic cells in homeostasis. Nat Immunol 16, 907–917, doi:10.1038/ni.3253 (2015). [PubMed: 26287597]

4. Hong S, Dissing-Olesen L & Stevens B New insights on the role of microglia in synaptic pruning in health and disease. Curr Opin Neurobiol 36, 128–134, doi:10.1016/j.conb.2015.12.004 (2016). [PubMed: 26745839]

5. Vargas ME & Barres BA Why is Wallerian degeneration in the CNS so slow? Annu Rev Neurosci 30, 153–179, doi:10.1146/annurev.neuro.30.051606.094354 (2007). [PubMed: 17506644]

6. Chao MP et al. Anti-CD47 antibody synergizes with rituximab to promote phagocytosis and eradicate non-Hodgkin lymphoma. Cell 142, 699–713, doi: 10.1016/j.cell.2010.07.044 (2010). [PubMed: 20813259]

7. Chen J et al. SLAMF7 is critical for phagocytosis of haematopoietic tumour cells via Mac-1 integrin. Nature 544, 493–497, doi:10.1038/nature22076 (2017). [PubMed: 28424516]

8. Ziegenfuss JS, Doherty J & Freeman MR Distinct molecular pathways mediate glial activation and engulfment of axonal debris after axotomy. Nat Neurosci 15, 979–987, doi:10.1038/nn.3135 (2012). [PubMed: 22706267]

9. Juncadella IJ et al. Apoptotic cell clearance by bronchial epithelial cells critically influences airway inflammation. Nature 493, 547–551, doi:10.1038/nature11714 (2013). [PubMed: 23235830]

10. Chung WS et al. Astrocytes mediate synapse elimination through MEGF10 and MERTK pathways. Nature 504, 394–400, doi:10.1038/nature12776 (2013). [PubMed: 24270812]

11. Freeman SA & Grinstein S Phagocytosis: receptors, signal integration, and the cytoskeleton. Immunol Rev 262, 193–215, doi:10.1111/imr.12212 (2014). [PubMed: 25319336]

12. Diakonova M, Bokoch G & Swanson JA Dynamics of cytoskeletal proteins during Fcgamma receptor-mediated phagocytosis in macrophages. Mol Biol Cell 13, 402–411, doi:10.1091/mbc. 01-05-0273 (2002). [PubMed: 11854399]

13. Fairn GD & Grinstein S How nascent phagosomes mature to become phagolysosomes. Trends Immunol 33, 397–405, doi:10.1016/j.it.2012.03.003 (2012). [PubMed: 22560866]

14. Swanson JA Shaping cups into phagosomes and macropinosomes. Nat Rev Mol Cell Biol 9, 639–649, doi:10.1038/nrm2447 (2008). [PubMed: 18612320]

15. Hedgecock EM, Sulston JE & Thomson JN Mutations affecting programmed cell deaths in the nematode Caenorhabditis elegans. Science 220, 1277–1279 (1983). [PubMed: 6857247]

16. Ellis RE, Jacobson DM & Horvitz HR Genes required for the engulfment of cell corpses during programmed cell death in Caenorhabditis elegans. Genetics 129, 79–94 (1991). [PubMed: 1936965]

17. Gumienny TL et al. CED-12/ELMO, a novel member of the CrkII/Dock180/Rac pathway, is required for phagocytosis and cell migration. Cell 107, 27–41 (2001). [PubMed: 11595183]

18. Tosello-Trampont AC, Brugnera E & Ravichandran KS Evidence for a conserved role for CRKII and Rac in engulfment of apoptotic cells. J Biol Chem 276, 13797–13802, doi:10.1074/jbc.M011238200 (2001). [PubMed: 11297528]

19. Logan MA et al. Negative regulation of glial engulfment activity by Draper terminates glial responses to axon injury. Nat Neurosci 15, 722–730, doi:10.1038/nn.3066 (2012). [PubMed: 22426252]

20. Silva E, Au-Yeung HW, Van Goethem E, Burden J & Franc NC Requirement for a Drosophila E3-ubiquitin ligase in phagocytosis of apoptotic cells. Immunity 27, 585–596, doi:10.1016/j.immuni. 2007.08.016 (2007). [PubMed: 17936033]

21. Garver LS, Wu J & Wu LP The peptidoglycan recognition protein PGRP-SC1a is essential for Toll signaling and phagocytosis of Staphylococcus aureus in Drosophila. Proc Natl Acad Sci U S A 103, 660–665, doi:10.1073/pnas.0506182103 (2006). [PubMed: 16407137]

22. Shen K, Sidik H & Talbot WS The Rag-Ragulator Complex Regulates Lysosome Function and Phagocytic Flux in Microglia. Cell Rep 14, 547–559, doi:10.1016/j.celrep.2015.12.055 (2016). [PubMed: 26774477]

23. Kocks C et al. Eater, a transmembrane protein mediating phagocytosis of bacterial pathogens in Drosophila. Cell 123, 335–346, doi:10.1016/j.cell.2005.08.034 (2005). [PubMed: 16239149]

24. Ramet M, Manfruelli P, Pearson A, Mathey-Prevot B & Ezekowitz RA Functional genomic analysis of phagocytosis and identification of a Drosophila receptor for E. coli. Nature 416, 644–648, doi:10.1038/nature735 (2002). [PubMed: 11912489]

25. Philips JA, Rubin EJ & Perrimon N Drosophila RNAi screen reveals CD36 family member required for mycobacterial infection. Science 309, 1251–1253, doi:10.1126/science.1116006 (2005). [PubMed: 16020694]

26. Stroschein-Stevenson SL, Foley E, O'Farrell PH & Johnson AD Identification of Drosophila gene products required for phagocytosis of Candida albicans. PLoS Biol 4, e4, doi:10.1371/journal.pbio.0040004 (2006). [PubMed: 16336044]

27. Mali P et al. RNA-guided human genome engineering via Cas9. Science 339, 823–826, doi: 10.1126/science.1232033 (2013). [PubMed: 23287722]

28. Jinek M et al. RNA-programmed genome editing in human cells. Elife 2, e00471, doi:10.7554/eLife.00471 (2013).

29. Cong L et al. Multiplex genome engineering using CRISPR/Cas systems. Science 339, 819–823, doi:10.1126/science.1231143 (2013). [PubMed: 23287718]

30. Adamson B et al. A Multiplexed Single-Cell CRISPR Screening Platform Enables Systematic Dissection of the Unfolded Protein Response. Cell 167, 1867–1882 e1821, doi: 10.1016/j.cell. 2016.11.048 (2016). [PubMed: 27984733]

31. Koike-Yusa H, Li Y, Tan EP, Velasco-Herrera Mdel C & Yusa K Genome-wide recessive genetic screening in mammalian cells with a lentiviral CRISPR-guide RNA library. Nat Biotechnol 32, 267–273, doi:10.1038/nbt.2800 (2014). [PubMed: 24535568]

32. Morgens DW et al. Genome-scale measurement of off-target activity using Cas9 toxicity in high-throughput screens. Nat Commun 8, 15178, doi:10.1038/ncomms15178 (2017). [PubMed: 28474669]

33. Parnas O et al. A Genome-wide CRISPR Screen in Primary Immune Cells to Dissect Regulatory Networks. Cell 162, 675–686, doi: 10.1016/j.cell.2015.06.059 (2015). [PubMed: 26189680]

34. Shalem O et al. Genome-scale CRISPR-Cas9 knockout screening in human cells. Science 343, 84–87, doi:10.1126/science.1247005 (2014). [PubMed: 24336571]

35. Wang T, Wei JJ, Sabatini DM & Lander ES Genetic screens in human cells using the CRISPR-Cas9 system. Science 343, 80–84, doi:10.1126/science.1246981 (2014). [PubMed: 24336569]

36. Zhou Y et al. High-throughput screening of a CRISPR/Cas9 library for functional genomics in human cells. Nature 509, 487–491, doi:10.1038/nature13166 (2014). [PubMed: 24717434]

37. Wang L et al. High-Throughput Functional Genetic and Compound Screens Identify Targets for Senescence Induction in Cancer. Cell Rep 21, 773–783, doi:10.1016/j.celrep.2017.09.085 (2017). [PubMed: 29045843]

38. Larrick JW, Fischer DG, Anderson SJ & Koren HS Characterization of a human macrophage-like cell line stimulated in vitro: a model of macrophage functions. J Immunol 125, 6–12 (1980). [PubMed: 7381211]

39. Morgens DW, Deans RM, Li A & Bassik MC Systematic comparison of CRISPR/Cas9 and RNAi screens for essential genes. Nat Biotechnol 34, 634–636, doi:10.1038/nbt.3567 (2016). [PubMed: 27159373]

40. Rotty JD et al. Arp2/3 Complex Is Required for Macrophage Integrin Functions but Is Dispensable for FcR Phagocytosis and In Vivo Motility. Dev Cell 42, 498–513 e496, doi:10.1016/j.devcel. 2017.08.003 (2017). [PubMed: 28867487]

41. Bassik MC et al. A systematic mammalian genetic interaction map reveals pathways underlying ricin susceptibility. Cell 152, 909–922, doi: 10.1016/j.cell.2013.01.030 (2013). [PubMed: 23394947]

42. Brumell JH et al. Expression of the protein kinase C substrate pleckstrin in macrophages: association with phagosomal membranes. J Immunol 163, 3388–3395 (1999). [PubMed: 10477609]

43. Ma AD & Abrams CS Pleckstrin induces cytoskeletal reorganization via a Rac-dependent pathway. J Biol Chem 274, 28730–28735 (1999). [PubMed: 10497244]

44. Roux KJ, Kim DI, Raida M & Burke B A promiscuous biotin ligase fusion protein identifies proximal and interacting proteins in mammalian cells. J Cell Biol 196, 801–810, doi:10.1083/jcb. 201112098 (2012). [PubMed: 22412018]

45. Bradley WD, Hernandez SE, Settleman J & Koleske AJ Integrin signaling through Arg activates p190RhoGAP by promoting its binding to p120RasGAP and recruitment to the membrane. Mol Biol Cell 17, 4827–4836, doi:10.1091/mbc.E06-02-0132 (2006). [PubMed: 16971514]

46. Jongstra-Bilen J & Jongstra J Leukocyte-specific protein 1 (LSP1): a regulator of leukocyte emigration in inflammation. Immunol Res 35, 65–74, doi:10.1385/IR:35:1:65 (2006). [PubMed: 17003510]

47. Schlam D et al. Phosphoinositide 3-kinase enables phagocytosis of large particles by terminating actin assembly through Rac/Cdc42 GTPase-activating proteins. Nat Commun 6, 8623, doi: 10.1038/ncomms9623 (2015). [PubMed: 26465210]

48. Kihara A Very long-chain fatty acids: elongation, physiology and related disorders. J Biochem 152, 387–395, doi:10.1093/jb/mvs105 (2012). [PubMed: 22984005]

49. Collins SR et al. Using light to shape chemical gradients for parallel and automated analysis of chemotaxis. Mol Syst Biol 11, 804, doi:10.15252/msb.20156027 (2015). [PubMed: 25908733]

50. Kajkowski EM et al. beta-Amyloid peptide-induced apoptosis regulated by a novel protein containing a g protein activation module. J Biol Chem 276, 18748–18756, doi:10.1074/jbc.M011161200 (2001). [PubMed: 11278849]

51. Jakobsdottir J et al. Rare Functional Variant in TM2D3 is Associated with Late-Onset Alzheimer's Disease. PLoS Genet 12, e1006327, doi:10.1371/journal.pgen.1006327 (2016).

52. Stine WB, Jungbauer L, Yu C & LaDu MJ Preparing synthetic Abeta in different aggregation states. Methods Mol Biol 670, 13–32, doi:10.1007/978-1-60761-744-0_2 (2011). [PubMed: 20967580]

53. Zhang Y et al. An RNA-sequencing transcriptome and splicing database of glia, neurons, and vascular cells of the cerebral cortex. J Neurosci 34, 11929–11947, doi:10.1523/JNEUROSCI. 1860-14.2014 (2014). [PubMed: 25186741]

54. Uusimaa J et al. NHLRC2 variants identified in patients with fibrosis, neurodegeneration, and cerebral angiomatosis (FINCA): characterisation of a novel cerebropulmonary disease. Acta Neuropathol 135, 727–742, doi:10.1007/s00401-018-1817-z (2018). [PubMed: 29423877]

55. Nishi K et al. ROS-induced cleavage of NHLRC2 by caspase-8 leads to apoptotic cell death in the HCT116 human colon cancer cell line. Cell Death Dis 8, 3218, doi:10.1038/s41419-017-0006-7 (2017). [PubMed: 29242562]

56. Horsthemke M et al. Multiple roles of filopodial dynamics in particle capture and phagocytosis and phenotypes of Cdc42 and Myo10 deletion. J Biol Chem 292, 7258–7273, doi: 10.1074/jbc.M116.766923 (2017). [PubMed: 28289096]

Methods-only References:

57. Larocca JN & Norton WT Isolation of myelin. Curr Protoc Cell Biol Chapter 3, Unit3 25, doi: 10.1002/0471143030.cb0325s33 (2007).

58. Mosser DM & Zhang X Measuring opsonic phagocytosis via Fcgamma receptors and complement receptors on macrophages. Curr Protoc Immunol Chapter 14, Unit 14 27, doi: 10.1002/0471142735.im1427s95 (2011).

59. Dunkley PR, Jarvie PE & Robinson PJ A rapid Percoll gradient procedure for preparation of synaptosomes. Nat Protoc 3, 1718–1728, doi:10.1038/nprot.2008.171 (2008). [PubMed: 18927557]

60. Kampmann M, Bassik MC & Weissman JS Integrated platform for genome-wide screening and construction of high-density genetic interaction maps in mammalian cells. Proc Natl Acad Sci U S A 110, E2317–2326, doi:10.1073/pnas.1307002110 (2013). [PubMed: 23739767]

61. Kramer NJ et al. CRISPR-Cas9 screens in human cells and primary neurons identify modifiers of C9ORF72 dipeptide-repeat-protein toxicity. Nat Genet 50, 603–612, doi:10.1038/s41588-018-0070-7 (2018). [PubMed: 29507424]

62. Liu N et al. Selective silencing of euchromatic L1s revealed by genome-wide screens for L1 regulators. Nature 553, 228–232, doi:10.1038/nature25179 (2018). [PubMed: 29211708]

63. Li W et al. MAGeCK enables robust identification of essential genes from genome-scale CRISPR/Cas9 knockout screens. Genome Biol 15, 554, doi:10.1186/s13059-014-0554-4 (2014). [PubMed: 25476604]
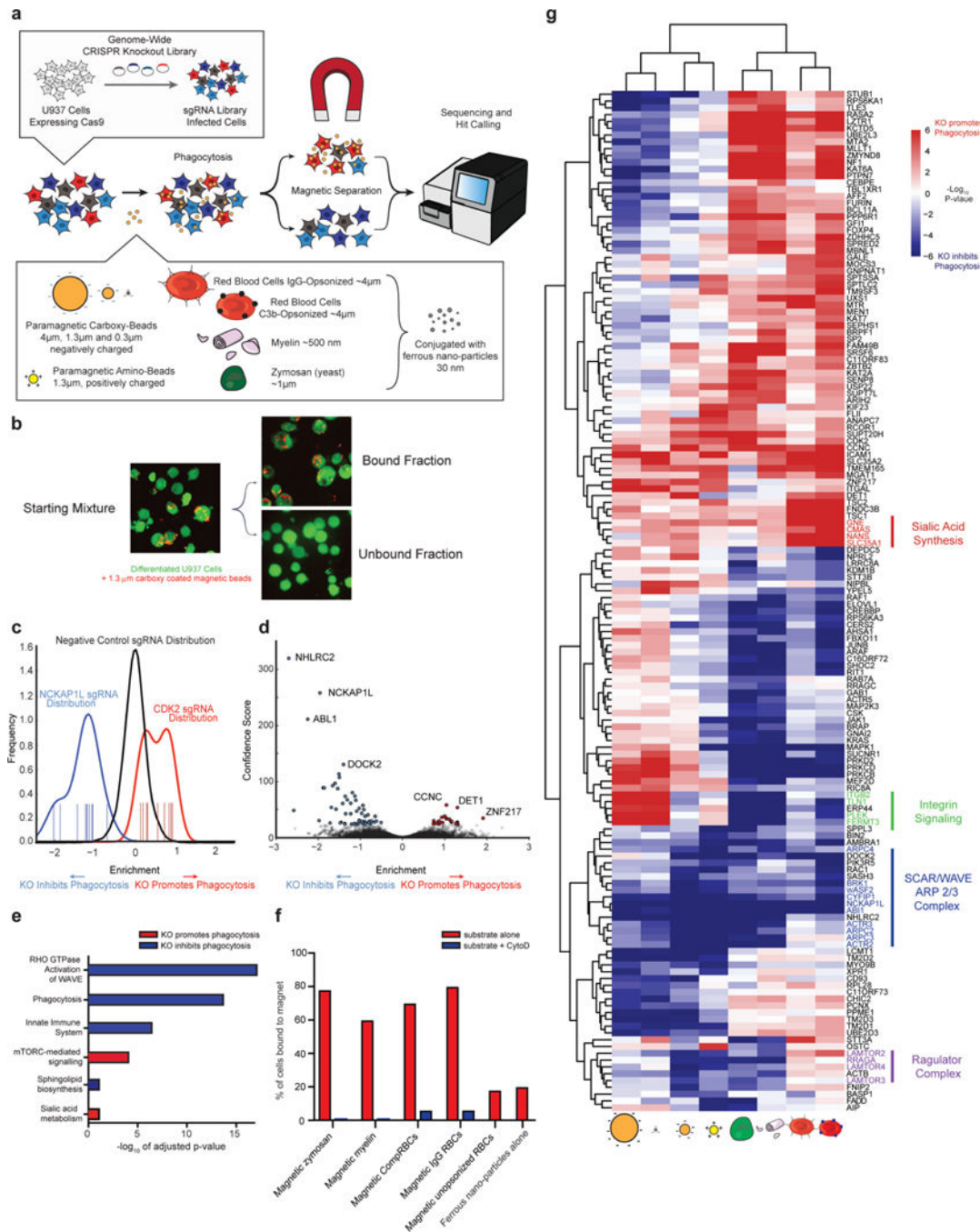
Figure 1. Genome-wide CRISPR screening for genetic regulators of phagocytosis.

a. Schematic of phagocytosis screening strategy using magnetic separation. Labeling with ferrous nano-particles enables magnetic separation screening of diverse substrates, and comparison with paramagnetic beads of different size and charge.

b. Confocal microscopy demonstrates efficient magnetic separation of phagocytosing and non- phagocytosing cells from a mixed population (1.3 μm magnetic beads). Representative of 4 independent experiments.

c. sgRNA distributions for two example hits and the distribution of negative control sgRNAs from a genome-wide phagocytosis screen using 1.3 μm magnetic beads. A positive value indicates enrichment in the magnet-bound fraction, and a negative value indicates enrichment in the unbound fraction. Enrichment of 10 sgRNAs targeting NCKAP1L and CDK2 are represented with blue and red vertical lines, respectively. The distribution ~10,000 negative controls is shown in black.

d. Volcano plot of all genes indicating the effect and confidence scores for a genome-wide phagocytosis screen using 1.3 μm magnetic beads. Effect and confidence scores are determined by casTLE. The 85 genes passing 10% FDR for inhibiting or promoting phagocytosis are highlighted in blue and red respectively.

e. Select Reactome categories enriched in the 85 genes that pass the 10% FDR cutoff as determined by casTLE (Reactome category IDs listed in methods – some categories are abbreviated).

f. Phagocytosis of diverse substrates is actin dependent. Cells were pretreated with the actin polymerization inhibitor cytochalasin D (CytoD) before exposure to ferrous nano-particle-labeled substrates, and binding to the magnetic column was compared to uninhibited cells.

g. Comparison of phagocytosis screen results with eight different substrates using unbiased hierarchical clustering, based on 150 genes that reached a <5% FDR cutoff as determined by casTLE in at least three screens. Select, functionally related sets are highlighted.
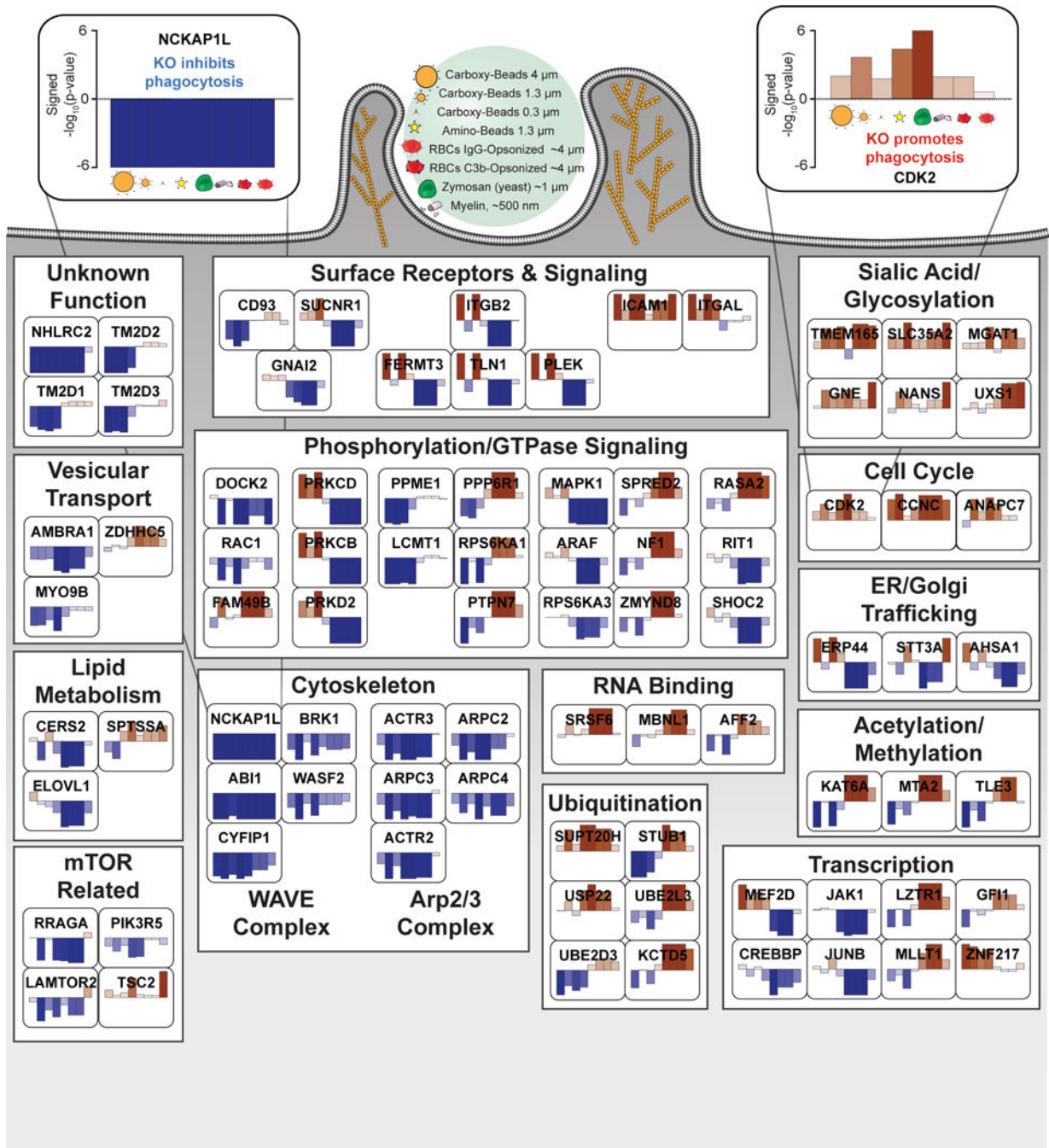
Figure 2. Putative modifiers of phagocytosis of diverse substrates from eight genome-wide screens.

Bar plots represent the signed $\log_{10}$ of the p-value for each gene for each substrate as calculated by casTLE using two replicate screens for each of eight different substrates. Each gene represented passed a 5% FDR threshold in at least three genome-wide phagocytosis screens. A negative value (blue bars) indicates that the gene knockout inhibits phagocytosis, and a positive value (red bars) indicates that the gene knockout promotes phagocytosis. Annotations of cellular processes and compartments were based on literature and GO-term assignments.
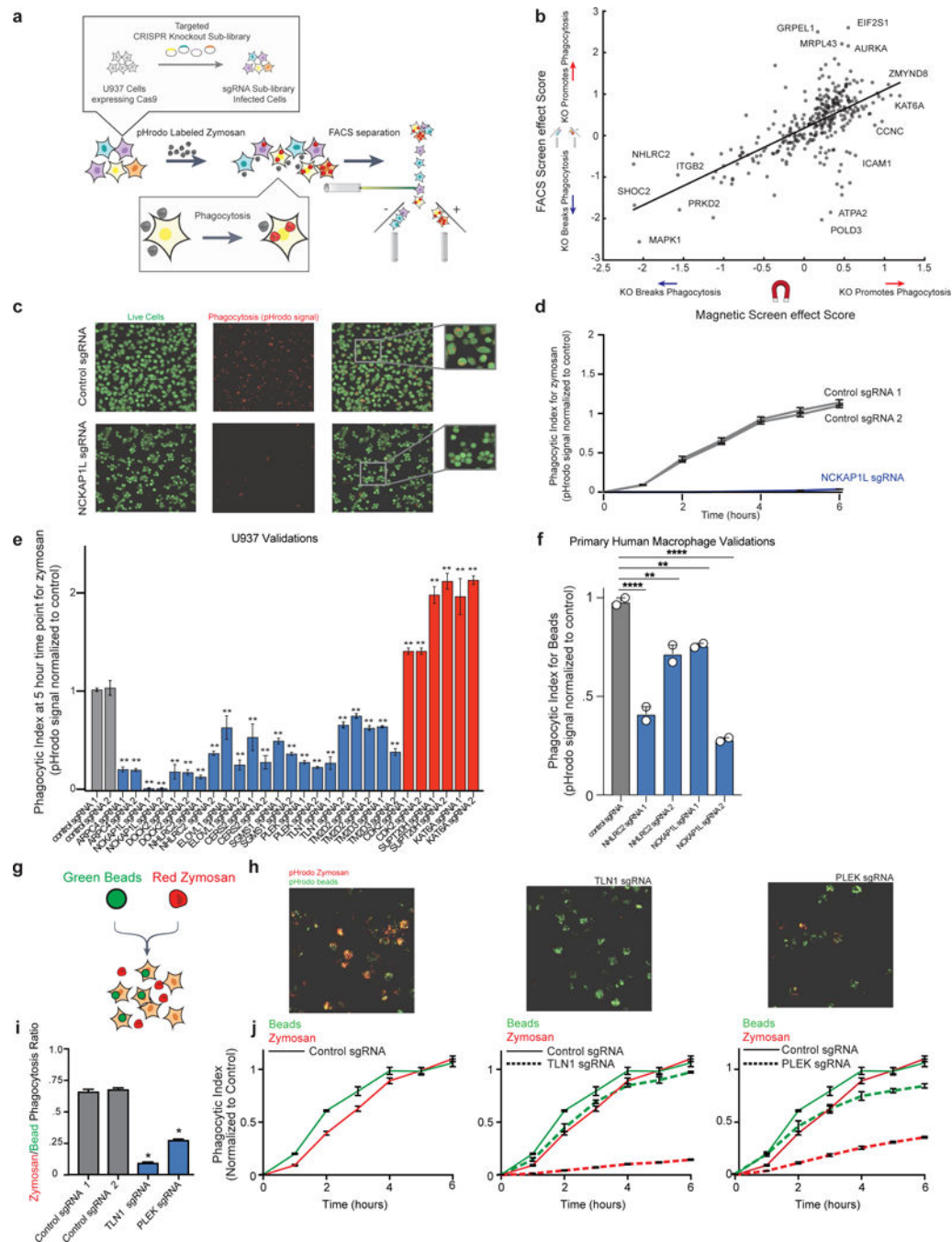
Figure 3. Orthogonal measurements of phagocytosis validate magnetic screen results.
a. Design of FACS-based validation screen. Differentiated U937 cells containing a custom sgRNA library targeting 322 genes identified in the genome-wide screens were FACS-sorted based on fluorescence signal from pHrodo-labeled zymosan.
b. Correlation of casTLE effect scores between FACS and magnetic separation screens using the 322-gene custom sgRNA library.

c. U937 cells expressing a NCKAP1L sgRNA treated with pHrodo-labeled zymosan (red). Live cells were labeled with Calcein AM (green). Representative of six independent experiments. Scale bars = 50 μm.

d. Automated live cell microscopy was used to monitor signal from pHrodo zymosan over time. A phagocytic index was calculated by measuring the total area of pHrodo signal divided by the total live cell area, then normalized to the average value of the control lines at 5 hr. Values represent mean ± S.E.M of n=4 replicate wells.

e. Summary of additional validations. The phagocytic index at 5 hr is presented. Values represent mean ± S.E.M of n=4 replicate wells. (**p< .01, *p< .05, two-way ANOVA with Dunnett's comparison to control sgRNA).

f. Validation in primary human macrophages. FACS measurement of pHrodo-labeled bead phagocytosis with either control sgRNA or sgRNAs targeting NCKAP1L or NHLRC2. Results are normalized to the maximal response by each independent donor. Values represent mean ± S.E.M of n=4 (NHLRC2 or NCKAP1L) or n=6 (Control) technical replicates. Dots represent averaged technical replicates across n= 2 biological donors. **p<. 01, ****p<.0001 (one-way ANOVA with multiple-comparisons correction).

g. Schematic for competitive phagocytosis assay to validate substrate specific regulators of phagocytosis.

h. Example images from competitive phagocytosis assays of zymosan (red) and 1.3 μm beads (green) in U937 cells expressing a control sgRNA, TLN1 sgRNA, or PLEK sgRNA. Images are representative of two independent experiments. Scale bars = 10 μm.

i. Ratio of total red area (zymosan) to total green area (bead) at 5 hours in cells expressing control sgRNA or sgRNAs targeting TLN1 or PLEK. Values represent mean ± S.E.M. (*p<. 05, two-tailed t- test from n=4 technical replicates; results are representative of three independent experiments).

j. Phagocytic index of zymosan (red) and beads (green) in competitive phagocytosis assay over time. Values represent mean ± S.E.M of n=4 replicate wells; results are representative of three independent experiments.
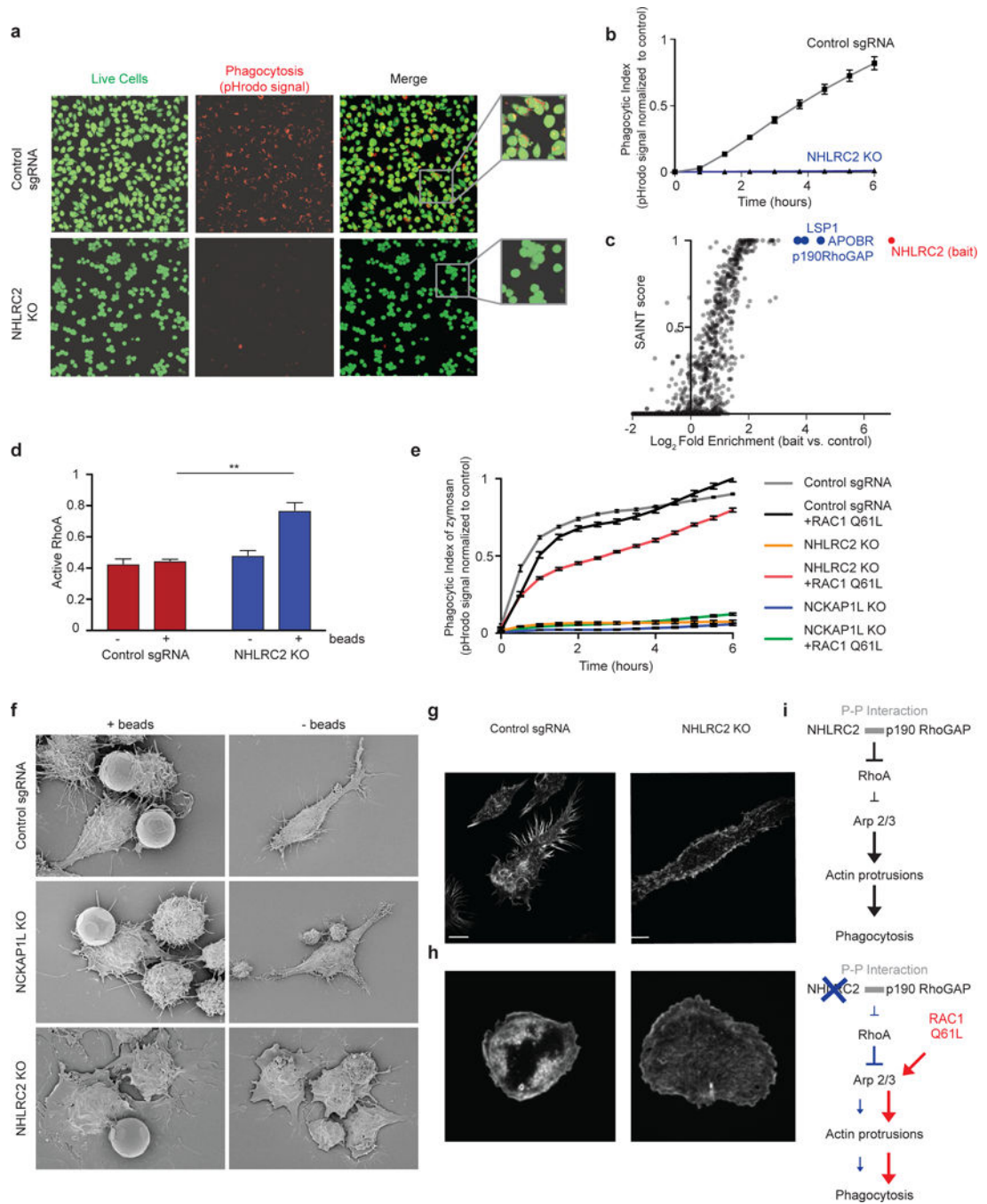
Figure 4. Loss of NHLRC2 inhibits phagocytosis through Rho/Rac1 signaling.

a. Clonally derived U937 cells with verified NHLRC2 knockout were labeled with Calcein AM (green) after 5 hr of exposure to pHrodo labeled zymosan (red). Representative of six independent experiments. Scale bar = 50 μm.

b. Phagocytic index (see Figure 3) of pHrodo labeled zymosan from control sgRNA expressing U937s and clonally derived NHLRC2 KO U937 cells. Values represent mean ± S.E.M. of n=4 replicate wells.

c. Results from BioID for NHLRC2. Enrichment of a protein in the NHLRC2-BirA pulldown versus BirA alone is plotted against the mean confidence score (SAINT score) (n=3 experimental replicates). The bait protein (NHLRC2) is highlighted in red and top protein interactors are highlighted in blue.

d. Quantification of active (GTP-bound) RhoA in RAW 264.7 cells expressing a control sgRNA (red) or confirmed *Nhlrc2* KO RAW 264.7 cells (blue) as determined by. ELISA signal was normalized against recombinant GTP-bound RhoA. Values represent mean ± S.E.M. of n=3 experimental replicates (**p<.005, two-tailed t-test).

e. Phagocytic index measurements using pHrodo labeled zymosan of RAW 264.7 cells expressing a control sgRNA (grey) with constitutively active (CA) RAC1 (black), *Nhlrc2* KO cell line (yellow) with active (CA) RAC1 (red), *Nckap1l* KO cell line (blue) with constitutively active (CA) RAC1 (green). Values represent mean ± S.E.M for n = 4 replicate wells.

f. Scanning electron microscopy of RAW 264.7 cells with control sgRNA (top row), *Nckap1l* KO (middle row), and *Nhlrc2* KO (bottom row) with (left) and without beads (right). Representative images of 3 experimental replicates. Scale bar = 2 μm

g. F-actin staining (AlexaFluor 488 phalloidin) of RAW 264.7 with control sgRNA (left) and *Nhlrc2* KO (right). Representative images of 3 experimental replicates. Scale bars = 10 μm.

h. F-actin staining of control sgRNA (left) and *Nhlrc2* KO (right) RAW 264.7 cells engaging IgG-coated coverslips during frustrated phagocytosis. Scale bars = 10 μm
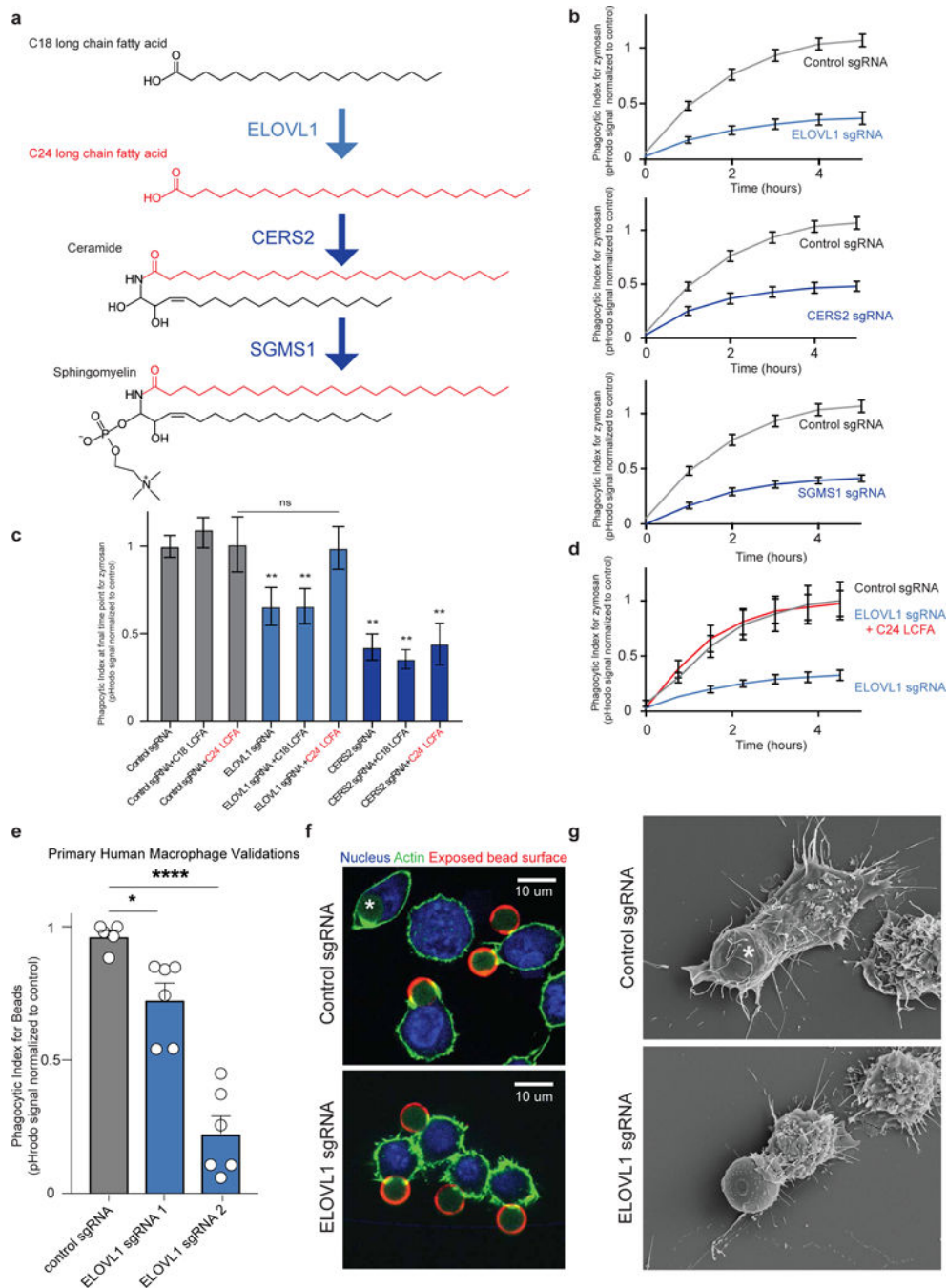
i. Model for role of NHLRC2 in phagocytosis.

Figure 5. Role for very long chain fatty acids (VLCFAs) in phagocytosis.
a. Genes identified in the genome-wide screens as required for phagocytosis (ELOVL1, CERS2, and SGMS1) participate in consecutive steps of a lipid biosynthetic pathway.
b. Validation of pathway members using automated microscopy. Phagocytosis was monitored over time as in Figure 3 using U937 cells containing the indicated guide and pHrodo-labeled zymosan. Values represent mean ± S.E.M, n=6 replicate wells.
c. Rescue of ELOVL1 deficiency by LCFA supplementation. Phagocytosis measured at 5 hr from U937 cells expressing control (grey), ELOVL1 (light blue), or CERS2 sgRNA (dark

blue) supplemented with C18 or C24 long chain fatty acids (LCFA). Values represent mean ± S.E.M, n = 6 replicate wells. (**p< .01, one-way ANOVA with Dunnett's comparison to control sgRNA).

d. Phagocytic index over time for U937 lines expressing a control sgRNA (grey), an ELOVL1 sgRNA (blue), or an ELOVL1 sgRNA and supplemented with C24 LCFA (red). Values represent mean ± S.E.M, n=4 replicate wells.

e. Validation of ELOVL1 phagocytic function in primary human macrophages. FACS measurement of the pHrodo-labeled zymosan phagocytosis by macrophages electroporated with either control sgRNA or sgRNAs targeting ELOVL1. Results normalized to the maximal response by each independent donor. Values represent mean ± S.E.M of n=5 (Ctrl or sgRNA 2) or n=6 (sgRNA 1) technical replicates. Experiments performed with n=3 biological donors. Dots represent technical replicates.*p<.05, ****p<.0001 (one-way ANOVA with multiple-comparisons correction).

f. RAW 264.7 cells expressing a control sgRNA (top) or ELOVL1 targeting sgRNA (bottom) were incubated with IgG-coated 7 μm beads for 10 minutes and fixed. IgG signal (red) marks bead surfaces unobstructed by cellular contact. Cells were stained with phalloidin (green) and Hoechst nuclear stain (blue). White asterisk marks a fully internalized bead. Representative of two independent experiments. Scale bars = 10 μm.

g. Scanning electron microscopy of RAW 264.7 cells expressing a control sgRNA (top) or ELOVL1 sgRNA (bottom) that were incubated with IgG-coated 7 μm beads for 10 minutes and fixed. White asterisk marks a fully internalized bead.
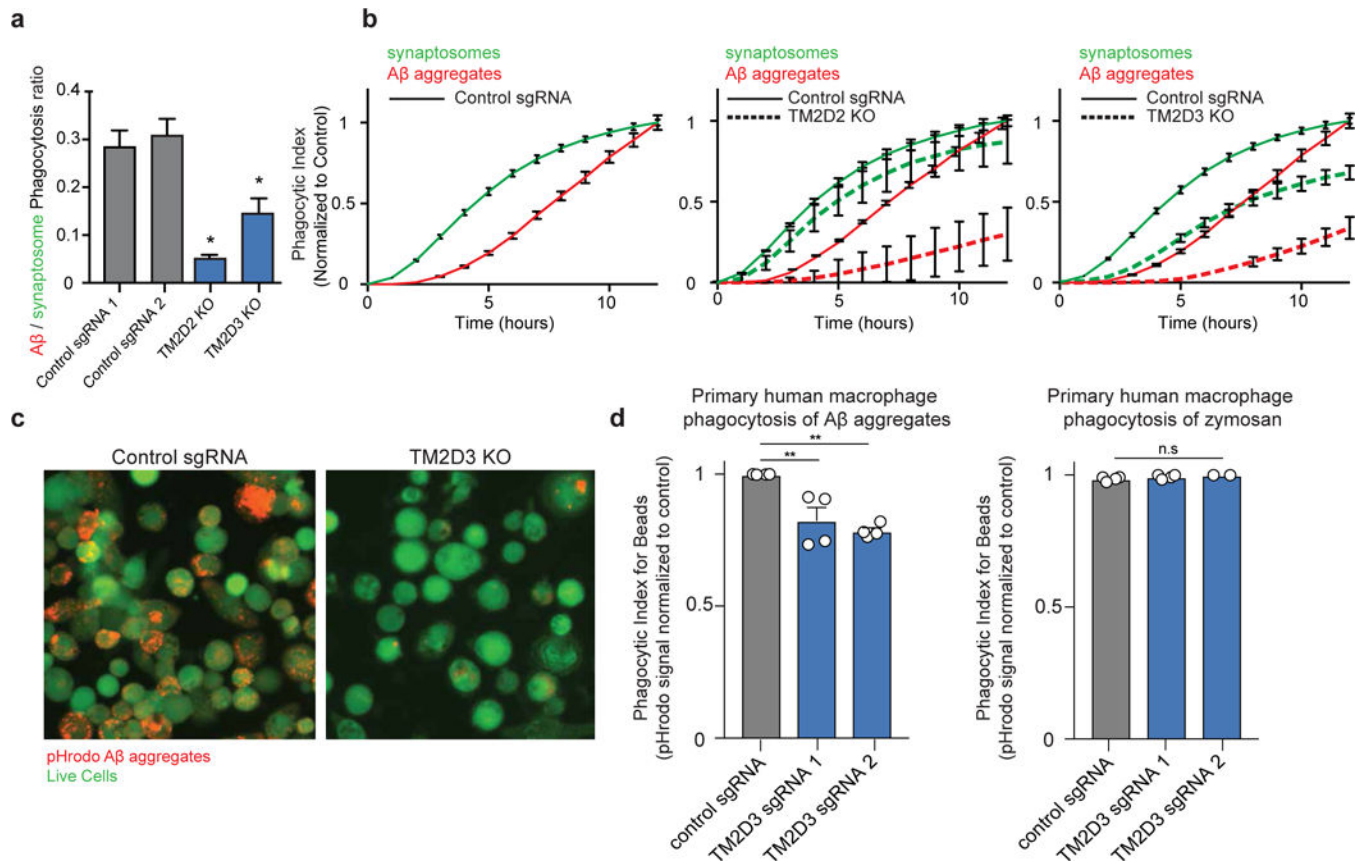
Figure 6. Identification of substrate specific regulators of phagocytosis.

a. Ratio of total red area (indicating phagocytosis of Amyloid β (Aβ) aggregates) to total green area (indicating phagocytosis of synaptosomes) at final time point of phagocytosis assay in cells expressing control sgRNA or confirmed U937 TM2D3 and TM2D2 clonal knockout lines. Values represent mean ± S.E.M. of n=4 replicate wells (*p<.05, two-tailed t-test).

b. Competitive phagocytosis assay in U937 cells expressing control sgRNAs or confirmed U937 TM2D3 and TM2D2 clonal knockout lines. Synaptosomes are labeled with pHrodo green and Amyloid β (Aβ) aggregates labeled with pHrodo red. Phagocytic index for each substrate measured over time using automated live cell imaging. Values represent mean ± S.E.M. of n=4 replicate wells (*p<.05, two-tailed t-test).

c. Phagocytosis of Amyloid β (Aβ) aggregates (labeled with pHrodo red) is impaired in confirmed clonal U937 TM2D3 knockout line when compare to U937s expressing control sgRNA. Live U937 cells labeled with Calcein AM (green). Representative of three independent experiments. Scale bar = 10 μm.

d. Validation in primary human macrophages of role of TM2D3 in Amyloid β (Aβ) aggregates and zymosan phagocytosis. Flow cytometry-based measurement of the phagocytosis of pHrodo-labeled Amyloid β (Aβ) aggregates or of pHrodo-labeled zymosan by genetically modified macrophages electroporated with either control sgRNA or sgRNAs targeting TM2D3. Results normalized to the maximal response by each independent donor. Values represent mean ± S.E.M of n=2–4 technical replicates. Experiments performed with

n=2 biological donors. Dots represent technical replicates. **p<.01. (one-way ANOVA with multiple-comparisons correction).